ACS APPLIED ENERGY MATERIALS

www.acsaem.org
Article

Improvement of Lithium-Ion Conductivity by Hf Substitution in Lithium Tantalum Phosphate ($LiTa_2PO_8$) Solid Electrolyte

Gen Hasegawa,* Youngseok Kim, Yoshinori Tanaka, Naoaki Kuwata,* Kunimitsu Kataoka, Takahisa Ohno, Junji Akimoto,* and Kazunori Takada

Cite This: *ACS Appl. Energy Mater.* 2024, 7, 10897−10905

ABSTRACT: $LiTa_2PO_8$, with a recently discovered framework structure and a bulk conductivity of 1.6×10^{-3} S cm^{-1}, exhibits high potential as an electrolyte material for solid-state batteries. We have improved the ionic conductivity of $LiTa_2PO_8$ via elemental substitution. In this study, we use ab initio molecular dynamics simulations to select the substituted elements and find that interstitial Li^+ ions improve Li^+ ion mobility in the bulk. Consequently, we synthesize $Li_{1+x}Ta_{2-x}Hf_xPO_8$, in which part of Ta^{5+} in $LiTa_2PO_8$ is substituted with Hf^{4+} for introducing interstitial Li^+ ions. $Li_{1.2}Ta_{1.8}Hf_{0.2}PO_8$ exhibits a total conductivity of 9.2×10^{-4} S cm^{-1} at 300 K, over twice higher than that of unsubstituted $LiTa_2PO_8$. Further, pulsed-field-gradient nuclear magnetic resonance indicates that the Li^+ ion diffusion coefficient of $Li_{1.2}Ta_{1.8}Hf_{0.2}PO_8$ in the bulk (2.0×10^{-8} cm^2 s^{-1} at 330 K) is twice as high as that of $LiTa_2PO_8$ (1.2×10^{-8} cm^2 s^{-1}), with the activation energy reduced from 0.30 to 0.27 eV. This improvement in the bulk diffusion can be attributed to the higher dimensionality of the conduction paths with introduced interstitial Li^+ ions.

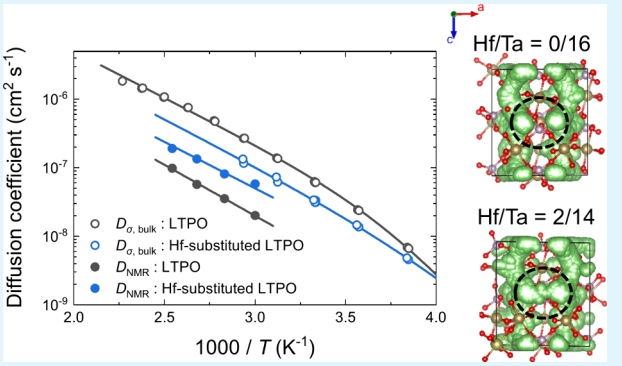

KEYWORDS: *$LiTa_2PO_8$, Hf-substitution, Solid-state batteries, Oxide solid electrolytes, Ionic conductors, PFG-NMR, Diffusion*

1. INTRODUCTION

Solid-state lithium batteries are expected to be the next-generation energy storage devices. Various lithium-ion conducting materials have been developed as key materials for practical applications of solid-state lithium batteries. The highest conductivity among sulfide-based electrolytes reaches 10^{-2} S cm^{-1},[1,2] which is comparable to that of liquid electrolytes. Although solid-state batteries have been suffering from high interface resistance between the sulfide electrolytes and cathodes, it has been reduced by interposing a buffer layer between the electrolyte and cathode.[3,4] Thus, sulfide-based solid electrolytes are currently being developed for applications in electric vehicles.[5] However, sulfide-based electrolytes decompose in humid atmospheres and release harmful hydrogen sulfides.[6,7] In contrast, solid-oxide electrolytes are stable and thus usable in atmospheric conditions. Recently, garnet-type[8−12] and LISICON-type[13−15] oxide electrolytes have gained considerable research attention. However, such solid oxide electrolytes still have challenges to overcome,[16−19] so it is important to continue developing new materials.

Kim et al. reported $LiTa_2PO_8$ (LTPO) as a solid-state electrolyte with a new framework structure.[20] The total and bulk conductivities of LTPO are 2.5×10^{-4} and 1.6×10^{-3} S cm^{-1} at 25 °C, respectively. Ishigaki et al. confirmed the high bulk conductivity of LTPO using pulsed-field gradient nuclear magnetic resonance (PFG-NMR).[21,22] Ab initio molecular dynamics (MD) simulations suggested that LTPO has low-dimensional ionic conduction pathways.[23,24] Dai et al. examined the positions of the Li^+ ion sites in LTPO using the bond valence site model.[25] They demonstrated that the Li^+ ion conduction pathway in the LTPO is quasi-one-dimensional along the *c*-axis. The low-dimensional conduction pathways can reduce the grain boundary and bulk conductivity of polycrystalline materials because they are easily disconnected at antisite defects or grain boundaries.[24] There have been recent reports of elemental substitutions in LTPO that increase ionic conductivity, for example, the substitution of M^{4+} (Zr, Ce, Te) for Ta^{5+}[26−28] or the substitution of Si^{4+} for P^{5+}.[24]

In this study, we perform ab initio MD simulations to explore substitution elements that enhance the Li^+ ion diffusion in LTPO. The MD simulations suggest that introducing interstitial Li^+ ions increases the Li^+ ion diffusion coefficient. Based on this prediction, Ta^{5+} in LTPO is partially

Received: July 9, 2024
Revised: November 1, 2024
Accepted: November 4, 2024
Published: November 15, 2024

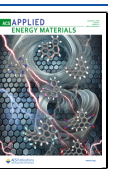

https://doi.org/10.1021/acsaem.4c01773
ACS Appl. Energy Mater. 2024, 7, 10897−10905

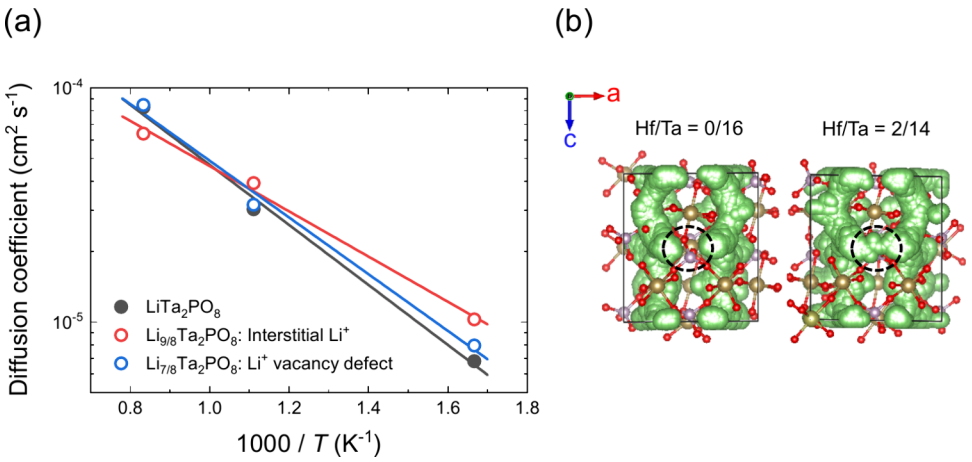

Figure 1. (a) Li^+ ion diffusion coefficients computed by MD calculations. Black indicates the diffusion coefficient for stoichiometric LTPO, red indicates the diffusion coefficient for LTPO with interstitial Li^+, and blue indicates the diffusion coefficient for LTPO with Li^+ vacancy defect. (b) Trajectories of Li^+ ions in Hf-substituted LTPO obtained by MD calculations at 600 K. Ta/Hf ratio represents the amount of Hf substitution in the unit cell ($8[Li_{1+x}Ta_{2-x}Hf_xPO_8]$).

substituted with Hf^{4+}. The substitution has increased the total conductivity by more than twice, and it has reached 9.2×10^{-4} S cm^{-1} in the Hf-substituted LTPO. In addition, PFG-NMR reveals that the bulk diffusion improves.

2. METHODS

2.1. Calculation of Elemental Substitution in LTPO. First-principles density functional theory calculations were performed using the Vienna ab initio simulation package (VASP),[29] where the projector-augmented wave (PAW) pseudopotentials[30] were considered, and exchange-correlation energy was treated using the Perdew–Burke–Ernzerhof gradient-corrected functional.[31] The bulk LTPO was modeled using a supercell containing 96 atoms with eight formula units. To study the structural properties, the wave functions were expanded into plane waves using a kinetic energy cutoff of 520 eV, with Brillouin zone integrations sampled using a $2 \times 2 \times 2$ k-point grid. The optimized lattice parameters of bulk LTPO were a = 9.84 Å, b = 11.71 Å, c = 10.91 Å, and β = 90.51°, consistent with the experiment values[20] within an error of 2%. To investigate the Li^+ diffusion in the LTPO systems, MD simulations were performed using a plane-wave energy cutoff of 400 eV and Γ-point sampling of the k-space with a time step of 1 fs in the canonical (NVT) ensemble. The defective LTPO with an interstitial Li^+ and a Li^+ vacancy was modeled using an 8-formula-unit supercell with a Li^+ ion being added and removed, respectively. For the Hf-substituted LTPO, we considered three different types of Ta sites (8f, 4e, and 4a) and their combinations as the Hf substitution sites. The Li^+ ion diffusivity was estimated from the atomic trajectories obtained by MD simulations at temperatures of 600–1200 K for 100 ps.

2.2. Synthesis of $Li_{1+x}Ta_{2-x}Hf_xPO_8$. $Li_{1+x}Ta_{2-x}Hf_xPO_8$ (x = 0.0, 0.1, 0.2) was prepared using the sol–gel method. $LiOH{\cdot}H_2O$ (Kojundo Chemical Laboratory) and $NH_4H_2PO_4$ (FUJIFILM Wako Pure Chemical Corporation) were dissolved in deionized water. $HfCl_4$ (FUJIFILM Wako Pure Chemical Corporation) and $TaCl_5$ (RARE METALLIC) were dissolved in anhydrous ethanol (FUJIFILM Wako Pure Chemical Corporation). The $HfCl_4$ solution, $TaCl_5$ solution, and LiOH aqueous solution were mixed, and the $NH_4H_2PO_4$ aqueous solution was added dropwise to the mixed solution. The composition of the mixed solution was as per the target composition, with only the LiOH aqueous solution mixed in excess of 10% of the target composition. The mixed solution was stirred at 353 K to accelerate gelation. Following the progression of the gelation of the solution, it was dried at 393 K for 15 h, with the resulting powder crushed in a mortar. The ground powder was calcined in an alumina crucible at 873 K for 12 h under an oxygen atmosphere to synthesize amorphous $Li_{1+x}Ta_{2-x}Hf_xPO_8$. The amorphous $Li_{1+x}Ta_{2-x}Hf_xPO_8$ powder was ball-milled with ethanol at 350 rpm for 16 h and dried at 353 K for 6 h, with the dried powder crushed in a mortar and vacuum-dried at 473 K for 15 h. The resulting powder was uniaxially pelletized at 70 MPa for 10 min and then sintered at 1273 K for 12 h under an oxygen atmosphere. The Inductively Coupled Plasma Atomic Emission Spectrometry (ICP-AES) measurements confirmed that the composition of the sintered pellets was consistent with the target composition (Supporting Information Table S1). The relative densities are 82%, 78%, and 92% for $LiTa_2PO_8$, $Li_{1.1}Ta_{1.9}Hf_{0.1}PO_8$, and $Li_{1.2}Ta_{1.8}Hf_{0.2}PO_8$, respectively.

2.3. Sample Characterization. Powder X-ray diffraction (XRD) was performed on crushed sintered pellets to analyze the crystal structures of the samples. The measurements were conducted using a SmartLab (Rigaku) at 40 kV and 30 mA with Cu Kα_1 radiation (λ = 1.54056 Å) monochromatized via a Johansson-type curved mirror. Scanning electron microscopy (SEM) and scanning transmission electron microscopy (STEM) were performed to observe the microstructure of the sintered pellets. The sample surfaces for the SEM measurements were ion-milled using an ArBrade5000 system (Hitachi High-Tech). A JEM-ARM 200F system (JEOL) was used for STEM, and energy-dispersive X-ray spectroscopy (STEM-EDS) was performed to obtain elemental imaging. The ionic conductivities were measured via impedance spectroscopy using a high-frequency impedance system (4990EDMS-120 K, TOYO) in frequency and temperature ranges of 20–10^8 Hz and 200–440 K, respectively. Gold electrodes were formed on the sintered pellets via sputtering. The activation energy E_a of conductivity σ was calculated using the Arrhenius equation,

$$\sigma T = \sigma_0 \cdot \exp\left(-\frac{E_a}{k_B T}\right) \quad (1)$$

where T is the absolute temperature, σ_0 is the pre-exponential factor, and k_B is the Boltzmann constant.

2.4. Li^+ Ion Diffusion Coefficient Measurements by PFG-NMR. Diffusion coefficients were measured at 273–93 K using an ECA-400 NMR system equipped with a diffusion probe (JEOL). The resonance frequency of the ^{7}Li nucleus was 155.4 MHz, the 90° pulse width was 16 μs, and the chemical shift for ^{7}Li was calibrated to 1 mol L^{-1} LiCl solution at 0 ppm. A pulsed gradient stimulated echo (PGSTE) sequence was used.[32] The decay of the PFG echo signal is generally expressed as the Stejskal–Tanner equation:[32,33]

$$\frac{S}{S_0} = \exp\left[-D\gamma^2 g^2 \delta^2 \left(\Delta - \frac{\delta}{3}\right)\right] \quad (2)$$

https://doi.org/10.1021/acsaem.4c01773
ACS Appl. Energy Mater. 2024, 7, 10897–10905

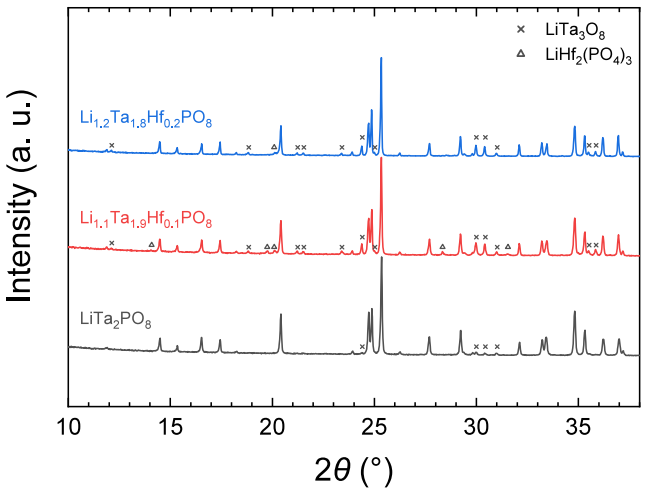

Figure 2. XRD patterns for LTPO, Hf01-LTPO, and Hf02-LTPO samples. All peaks without symbols are assignable to the LTPO phase. The crosses are peaks attributable to the $LiTa_3O_8$ phase, and the triangles are peaks attributable to the $LiHf_2(PO_4)_3$ phase.

where S/S_0 is the intensity ratio of the echo signal, D is the diffusion coefficient, γ is the gyromagnetic ratio, g is the magnitude of the magnetic field gradient, δ is the duration of the magnetic field gradient pulse, and Δ is the interval between the magnetic field gradient pulses (i.e., diffusion time). The range of g is 0.1−12 T m^{-1}. The values of δ and Δ were set to δ = 1 ms, Δ = 100 ms for LTPO and δ = 1 ms, Δ = 30 ms for Hf-substituted LTPO, based on the T_1 and T_2 relaxation time measurements (Supporting Information Figure S1).

3. RESULTS AND DISCUSSION

The MD simulations in this study suggest that introducing interstitial Li^+ ions enhances the Li^+ ion conduction in the LTPO. Figure 1a compares the Arrhenius plots of the Li^+ ion diffusion coefficients obtained via the MD simulations in LTPO, those with the Li^+ vacancies, and those with interstitial Li^+ ions. The term "interstitial Li" refers to the excess Li introduced by the Hf substitution, which was initially placed at the 4b site. After the MD calculation, the position of the excess Li will be indistinguishable from the original Li. The activation energy of LTPO with Li^+ vacancies (calculated to be 0.25 eV) is almost the same as that of normal LTPO. However, the interstitial Li^+ lowers the activation energy to 0.19 eV, indicating that introducing interstitial Li^+ improves the ionic conduction in LTPO.

First-principles calculations and MD simulations also suggest that the partial substitution of Ta^{5+} with Hf^{4+} that introduces interstitial Li^+ ions will enhance the ionic conduction in LTPO. The ionic radius of six-coordinate Hf^{4+} is 0.71 Å, close to that of six-coordinate Ta^{5+} (0.64 Å), and the decomposition energy is lower than 100 meV $atom^{-1}$ obtained by the first-principles calculations (Supporting Information Table S2). This result indicates that the Hf-substituted LTPO can be synthesized as a metastable phase. In undoped LTPO, a quasi-two-dimensional honeycomb framework of Li^+ ion diffusion pathways in the bc-plane has been reported.[23] The quasi-two-dimensional diffusion pathway is also confirmed by MD calculations in this study (Figure 1b left). Furthermore, MD simulations of Hf-substituted LTPO show that Hf substitution widens the cross-linking channels between the two-dimensional conduc-

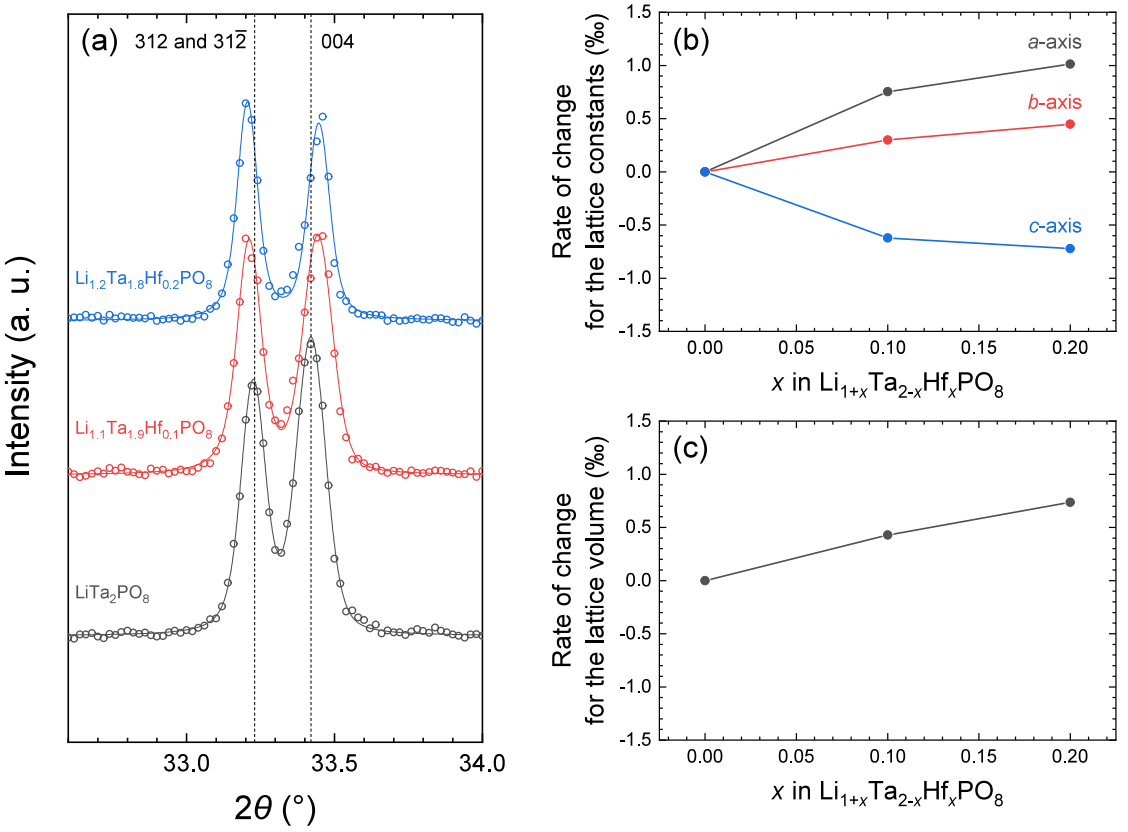

Figure 3. (a) XRD patterns of LTPO, Hf01-LTPO, and Hf02-LTPO samples in the 2θ range of 32.6−34.0°. (b) Rate of change for lattice parameter with Hf substitution. (c) Rate of change for the lattice volume with Hf substitution.

https://doi.org/10.1021/acsaem.4c01773
ACS Appl. Energy Mater. 2024, 7, 10897−10905

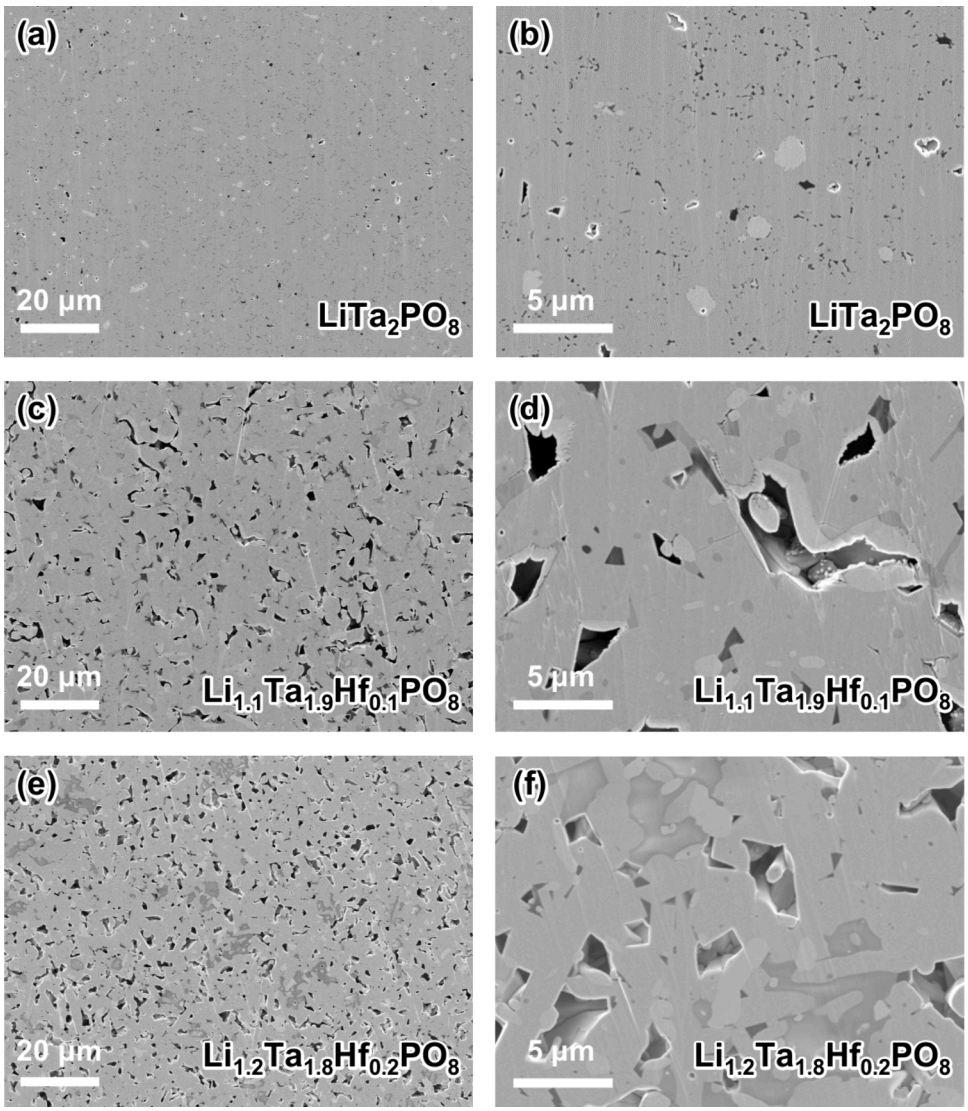

Figure 4. SEM cross-sectional images of (a, b) LTPO, (c, d) Hf01-LTPO, and (e, f) Hf02-LTPO samples.

tion pathways along the bc-plane, which will facilitate three-dimensional ionic conduction (Figure 1b right).

Figure 2 shows the XRD results of powders ground from the $LiTa_2PO_8$, $Li_{1.1}Ta_{1.9}Hf_{0.1}PO_8$ (Hf01-LTPO), and $Li_{1.2}Ta_{1.8}Hf_{0.2}PO_8$ (Hf02-LTPO) sintered samples. In all samples, most reflections are assigned to the LTPO structure in the space group $C2/c$,[20−22,25] and a small amount of $LiTa_3O_8$ appears as an impurity.[20,34] Furthermore, NASICON-type $LiHf_2(PO4)_3$[35−37] is observed as an impurity in the Hf01-LTPO and Hf02-LTPO samples. Results of the Rietveld analysis and the relative abundance of LTPO and impurities are shown in Supporting Information Figure S2 and Table S3. The XRD patterns in the 32.6−34.0° range are enlarged in Figure 3a, which indicates that Hf substitution shifts the 312 reflection to a lower angle and the 004 reflection to a higher angle. Figures 3b and 3c show the rates of change of the lattice constants and volume, respectively, calculated from the diffraction angles. The values of the lattice constants are shown in Supporting Information Table S4. With Hf substitution, the lattice constant c decreases, whereas the lattice constants a and b increase. The lattice volume also increased, which indicated that Hf^{4+}, with a larger ionic radius than Ta^{5+}, is substituted for Ta in LTPO. Such changes in lattice constants are consistent with the results of first-principles calculations (Supporting Information Table S5, Figure S3).

Figure 4 shows the SEM cross-sectional images of the LTPO, Hf01-LTPO, and Hf02-LTPO sintered samples. The Hf01-LTPO and Hf02-LTPO samples have larger particle sizes than the LTPO sample. Moreover, more impurities are present in the Hf-substituted samples than in the LTPO samples. STEM-EDS measurements confirm that these impurities correspond to those observed by XRD (Figure 5). Figure 5a shows the LTPO phase; an impurity of Ta oxide is observed, which is identified as $LiTa_3O_8$ by the XRD. In addition to these two phases, the STEM-EDS maps in Figure 5b suggest the presence of phosphate and hafnium phosphate in the Hf02-LTPO sample. The hafnium phosphate should be $LiHf_2(PO_4)_3$, which is detected in the XRD. On the other hand, the XRD pattern does not show the presence of any other phosphates, which is probably because the phosphate is amorphous lithium phosphate. The $LiHf_2(PO_4)$ and lithium phosphate have an ionic conductivity of 10^{-7}−10^{-5} S cm^{-1}[35,38,39] and are hence not expected to inhibit ionic

https://doi.org/10.1021/acsaem.4c01773
ACS Appl. Energy Mater. 2024, 7, 10897−10905

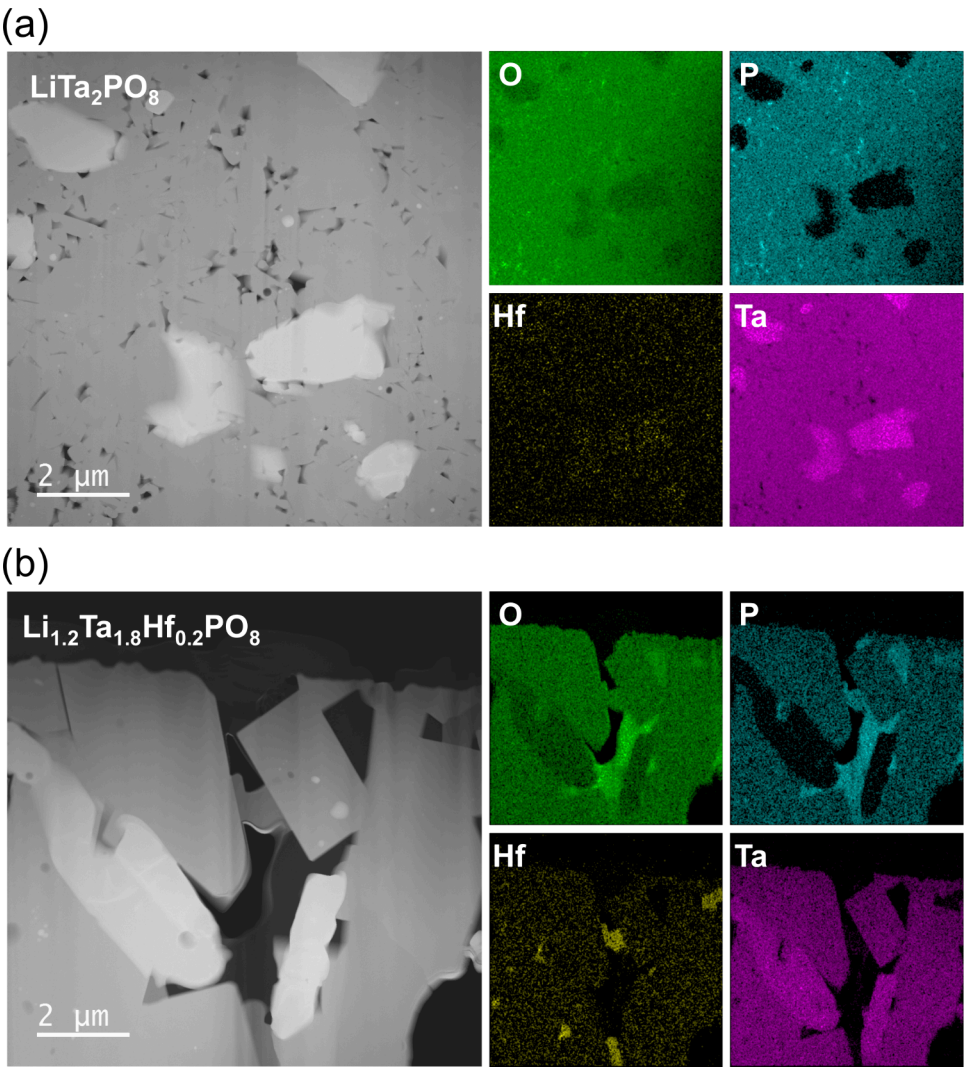

Figure 5. STEM-EDS images of (a) LTPO and (b) Hf02-LTPO samples. In the elemental mapping, O, P, Hf, and Ta are represented in green, cyan, yellow, and magenta, respectively.

conduction in the Hf-substituted LTPO samples significantly. Furthermore, point analysis of the EDS spectra in the LTPO phase indicates that Hf is substituted into the LTPO phase of the Hf02-LTPO sample (Supporting Information Figure S4). From the TEM-EDS analysis, the Hf composition in LTPO phase is determined as x = 0.009 and x = 0.076, for Hf01-LTPO and Hf02-LTPO, respectively. Kwatek et al. investigated the solubility limit in the Zr-substituted system $Li_{1+x}Zr_xTa_{2-x}PO_8$, which has a similar ion radius to Hf, in detail using ^{31}P MAS NMR and XRD.[26] The solubility limit is x = 0.055−0.075, which agrees with the concentration determined by TEM-EDS. Since Hf is similar in the ionic radius to Zr, the LTPO phase in the Hf01-LTPO and Hf02-LTPO samples seems to have a Hf composition close to the solubility limit.

Figures 6a−d show the Nyquist plots for the LTPO, Hf01-LTPO, and Hf02-LTPO samples at 300 K. The impedance diagram of the LTPO sample consists of two semicircles, corresponding to the bulk and grain boundary resistances, respectively, and a spike (Figure 6b). The total and bulk conductivities of LTPO sample are 3.9×10^{-4} S cm^{-1} and 2.5×10^{-3} S cm^{-1}, respectively, consistent with previous studies.[20−22] The total conductivities of both Hf01-LTPO and Hf02-LTPO samples are higher than that of the LTPO sample, with values of 8.6×10^{-4} S cm^{-1} and 9.2×10^{-4} S cm^{-1}, respectively. This increase in total conductivity is attributed to the reduction of grain boundary resistance caused by grain growth. Although the two semicircles clearly divided for the LTPO sample are merged for the Hf-substituted LTPO samples, deconvolution of the spectra using the equivalent circuit in Figure 6e yields a bulk conductivity of 1.4×10^{-3} S cm^{-1} for both Hf01-LTPO and Hf02-LTPO samples, lower than that of the LTPO sample—further discussed in comparison to the PFG-NMR results. As a reference, Supporting Information Table S6 shows the bulk and grain boundary capacitances for each sample at 300 K, calculated from the frequencies at the top of the semicircles. The impedance spectra for 200−400 K are shown in Supporting Information Figure S5. Figure 7 shows the temperature dependences of the total and bulk conductivities derived from the spectra. Figure 7a indicates that the Hf substitution decreases the activation energy of the total conductivity. The activation energies of total conductivity for the LTPO and Hf-substituted LTPO samples in the temperature range of 400−440 K are 0.35 and 0.26 eV, respectively, and 0.50 and 0.40 eV in the range of 200−220 K, respectively. These results are

https://doi.org/10.1021/acsaem.4c01773
ACS Appl. Energy Mater. 2024, 7, 10897−10905

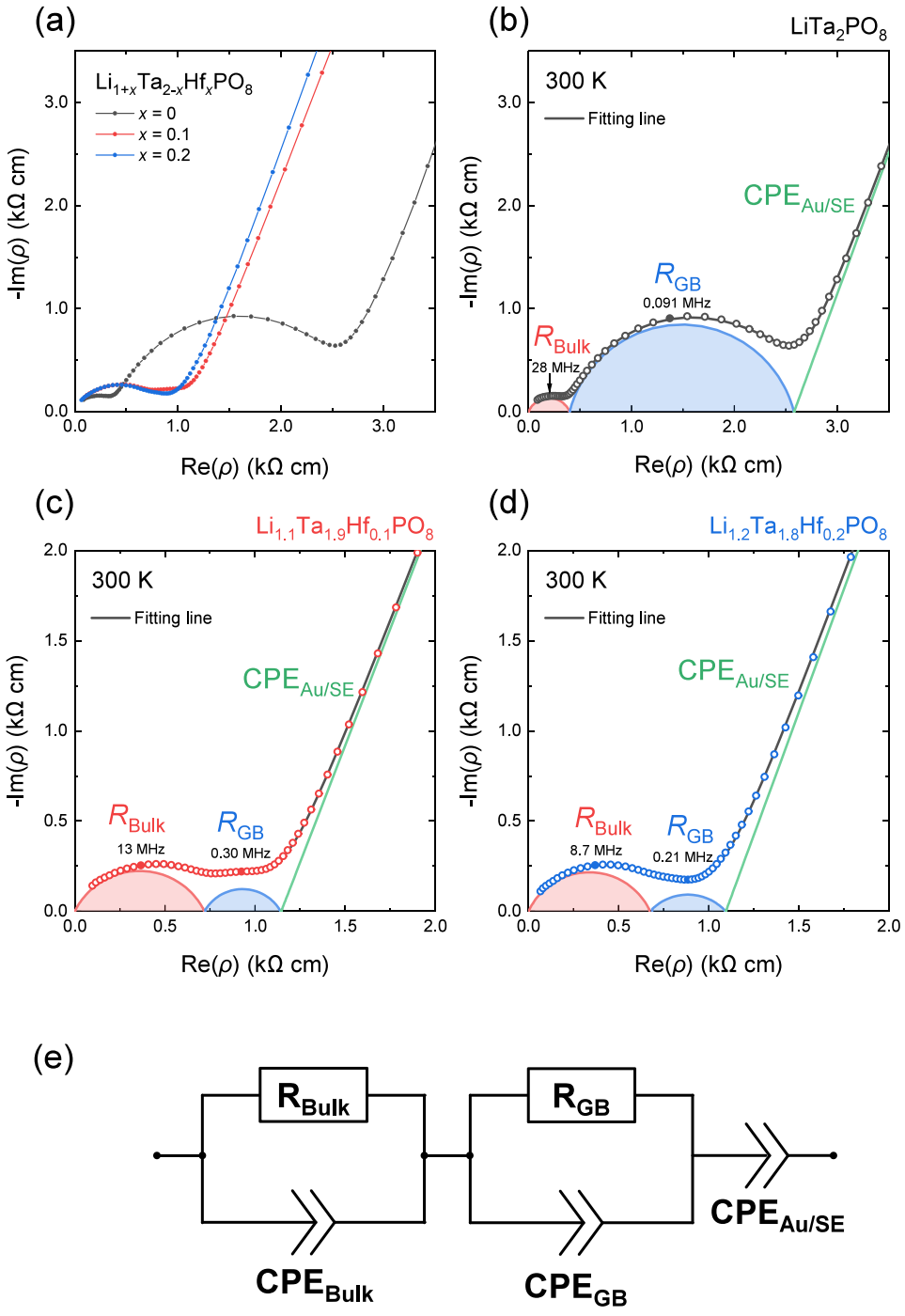

Figure 6. (a) Nyquist plots of LTPO, Hf01-LTPO, and Hf02-LTPO samples at 300 K. Impedance spectra of (b) LTPO, (c) Hf01-LTPO, and (d) Hf02-LTPO samples are deconvoluted using (e) the equivalent circuit. Closed circles in Figure 6b–d show the frequencies at the top of semicircles for bulk and grain boundary parts.

compared to those of previous studies on elemental substitution with Si,[24] Zr,[26] Te,[27] and Ce[28] in Supporting Information Figure S6. The Hf-substituted LTPO sample in this study has a total conductivity comparable to that of Si-substituted LTPO (the highest conductivity reported in previous studies). The activation energy for bulk conduction in the LTPO sample increases significantly below 250 K; however, this increase is suppressed in the Hf-substituted LTPO (Figure 7b). The temperature where the activation energy changes in the LTPO can be related to the phase transition temperature of LTPO, where the monoclinic angle β changes,[25] suggesting that Hf substitution suppresses the phase transformation of LTPO at low temperatures.

Figure 8 shows the temperature dependence of the bulk conductivity diffusion coefficient, $D_{\sigma,\,\mathrm{bulk}}$, obtained from the impedance spectroscopy and self-diffusion coefficient, D_{NMR}, determined by PFG-NMR for the LTPO and Hf02-LTPO samples. The conductivity diffusion coefficients are calculated from the bulk conductivity, σ_{bulk}, using the Nernst–Einstein equation:

https://doi.org/10.1021/acsaem.4c01773
ACS Appl. Energy Mater. 2024, 7, 10897–10905

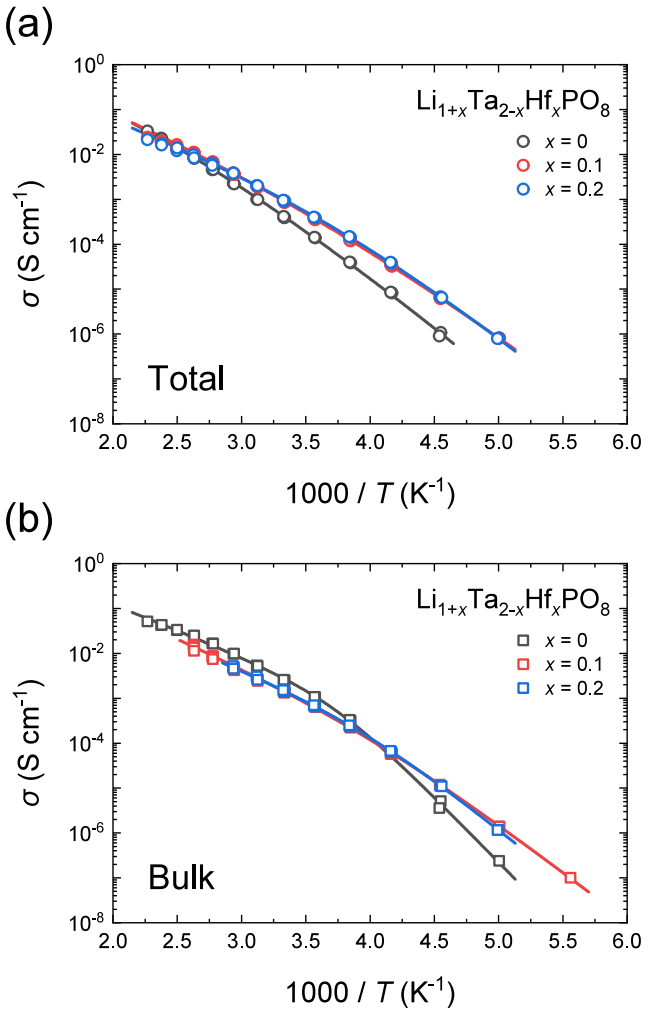

Figure 7. Arrhenius plots of (a) total and (b) bulk conductivities. Black indicates the LTPO sample, red indicates the Hf01-LTPO sample, and blue indicates the Hf02-LTPO sample.

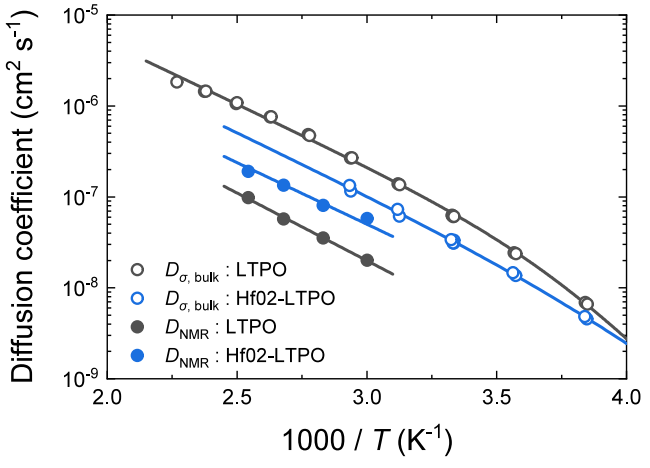

Figure 8. Arrhenius plots of self-diffusion coefficients D_{NMR} and conductivity diffusion coefficients $D_{\sigma,\,bulk}$. The filled circles are self-diffusion coefficients measured by PFG-NMR, and the open circles are conductivity diffusion coefficients determined from bulk conductivities. Black and blue indicate the LTPO and Hf02-LTPO samples, respectively.

$$D_{\sigma,\mathrm{bulk}} = \frac{k_B T}{e^2 z^2 n}\sigma_{\mathrm{bulk}} \tag{3}$$

where e is the elementary charge, z is the valence state of the carrier ion, and n is the carrier density. The value of n for the LTPO sample is 8.0×10^{21} cm^{-3}, determined based on the crystal structure,[20] while that for the Hf02-LTPO sample is set to be 1.2 times higher based on the ICP-AES result. The D_{NMR} value for LTPO is 2.0×10^{-8} cm^2 s^{-1} at 333 K, whereas that for Hf02-LTPO is 5.8×10^{-8} cm^2 s^{-1}, indicating that the Li$^+$ ion diffusion coefficient increases with Hf substitution. Ishigaki et al. reported a D_{NMR} value of 1.2×10^{-8} cm^2 s^{-1} for LTPO at 330 K,[21,22] consistent with the D_{NMR} value in this study. The activation energies in the 300−400 K range are 0.30 and 0.27 eV for the LTPO and Hf02-LTPO samples, respectively. The Hf substitution reduces the activation energy of bulk conduction in LTPO, as predicted by the MD simulations.

The Haven ratio ($D_{NMR}/D_{\sigma,\,bulk}$) of the LTPO sample is approximately 0.1, smaller than that of other oxide electrolytes,[11,39,40] probably owing to the strong correlation between the Li$^+$ ions[41,42] induced by the low-dimensional paths of Li$^+$ ion conduction. In the Hf02-LTPO sample, the Haven ratio is approximately 0.6, comparable to that of other oxide electrolytes. This increase in the Haven ratio can be interpreted in two ways. The first is the effect of impurities on bulk resistivity. Figure 6d shows the depression of the semicircle corresponding to the bulk resistive component, attributed to the inclusion of ionic conductive impurities in the Hf-substituted LTPO sample, such as the NASICON phase. Therefore, the actual bulk conductivity of the Hf-substituted LTPO phase can be much higher. In this case, the actual Haven ratio in the Hf-substituted LTPO phase would be less than 0.5. The second is the higher dimensionality of the Li conduction pathways upon Hf substitution, as shown in Figure 1b. Higher diffusion pathway dimensions generally result in a higher correlation factor for the self-diffusion coefficient.[43] In addition, the higher dimensionality of the conduction pathways is expected to reduce the many-body correlation between Li ions, affecting the ionic conductivity. While ions must move simultaneously with neighboring ions in a restricted conduction pathway, if the conduction pathway has multiple branches, ions can bypass neighboring ions, reducing the many-body correlations between ions. Therefore, higher dimensionality of conduction pathways can increase the Haven ratio via an increase in D_{NMR} and a decrease in D_σ. The larger Haven ratio of Hf-substituted LTPO suggests a higher dimensionality of the ionic conduction pathways.

In this study, we observed the effect of Hf substitution in LTPO, although a systematic composition dependence on physical properties such as EIS, T1, and T2 in Hf01-LTPO and Hf02-LTPO is not observed. There are two possible reasons for such composition dependence. The first is that the prepared composition exceeded the solubility limit of Hf, which leads to the generation of impurities inhibiting ionic conduction. The second is that LTPO is a metastable material. Thus, slight differences in the thermal history or atmosphere during synthesis can affect ionic conductivity. To further clarify the effect of Hf substitution in the bulk, it is necessary to quantify Hf substitution dependence in detail.

4. CONCLUSION

This study reveals that Hf substitution enhances ionic conduction in LTPO. The first-principles MD simulations

https://doi.org/10.1021/acsaem.4c01773
ACS Appl. Energy Mater. 2024, 7, 10897−10905

predict that introducing interstitial Li^+ ions decreases the activation energy for ionic conduction in LTPO. Hf substitution at the Ta sites employed in this study for generating interstitial Li^+ enhances grain growth and decreases grain boundary resistance, improving the total conductivity. PFG-NMR measurements have revealed that the Hf substitution reduces the activation energy and increases the diffusion coefficient in the bulk. A comparison of $D_{\sigma,\ bulk}$ and D_{NMR} between the substituted and unsubstituted LTPO suggests that the Hf substitution weakens the correlation effect between Li^+ ions originating from low-dimensional conduction pathways in LTPO. Thus, this study indicated that Hf substitution in LTPO can effectively improve conductivity.

■ ASSOCIATED CONTENT

Supporting Information

The Supporting Information is available free of charge at https://pubs.acs.org/doi/10.1021/acsaem.4c01773.

ICP-AES, T_1 and T_2 relaxation times, lattice constants calculated from the diffraction angles, phase stability and lattice constants via first-principles calculations, EDS spectra of the Hf L-edge in the LTPO phase via point analysis, temperature dependence of impedance spectra, and comparison with previous studies on total conductivity (PDF)

■ AUTHOR INFORMATION

Corresponding Authors

Gen Hasegawa − *Center for Green Research on Energy and Environmental Materials, National Institute for Materials Science (NIMS), Tsukuba, Ibaraki 305-0044, Japan;* orcid.org/0000-0002-9297-6902; Email: hasegawa.gen@nims.go.jp

Naoaki Kuwata − *Center for Green Research on Energy and Environmental Materials, National Institute for Materials Science (NIMS), Tsukuba, Ibaraki 305-0044, Japan;* orcid.org/0000-0002-0736-6967; Email: kuwata.naoaki@nims.go.jp

Junji Akimoto − *Center for Green Research on Energy and Environmental Materials, National Institute for Materials Science (NIMS), Tsukuba, Ibaraki 305-0044, Japan; National Institute of Advanced Industrial Science and Technology (AIST), Tsukuba, Ibaraki 305-8565, Japan; University of Tsukuba, Tsukuba, Ibaraki 305-8571, Japan;* orcid.org/0000-0001-9636-7680; Email: akimoto.junji@nims.go.jp

Authors

Youngseok Kim − *National Institute of Advanced Industrial Science and Technology (AIST), Tsukuba, Ibaraki 305-8565, Japan; University of Tsukuba, Tsukuba, Ibaraki 305-8571, Japan*

Yoshinori Tanaka − *Center for Green Research on Energy and Environmental Materials, National Institute for Materials Science (NIMS), Tsukuba, Ibaraki 305-0044, Japan*

Kunimitsu Kataoka − *National Institute of Advanced Industrial Science and Technology (AIST), Tsukuba, Ibaraki 305-8565, Japan;* orcid.org/0000-0001-5322-3011

Takahisa Ohno − *Center for Green Research on Energy and Environmental Materials, National Institute for Materials Science (NIMS), Tsukuba, Ibaraki 305-0044, Japan*

Kazunori Takada − *Center for Green Research on Energy and Environmental Materials, National Institute for Materials Science (NIMS), Tsukuba, Ibaraki 305-0044, Japan;* orcid.org/0000-0001-7568-1806

Complete contact information is available at: https://pubs.acs.org/10.1021/acsaem.4c01773

Notes

The authors declare no competing financial interest.

■ ACKNOWLEDGMENTS

This study was supported by the JST ALCA-SPRING Project, Grant Number JPMJAL1301, and the GteX Program, Grant Number JPMJGX23S2. This study was also supported by JSPS KAKENHI, Grant Number JP21H02033 (Grant-in-Aid for Scientific Research (B)). This study was partly supported by the Materials Processing Science project ("Materealize") of MEXT, Grant Number JPMXP0219207397. We thank Dr. Yasuhiro Shirai and Ms. Hiroko Ara for assisting with NMR measurement, and we also thank Mr. Keisuke Shinoda, Ms. Makiko Oshida, and Ms. Noriko Itoh for assisting with STEM and SEM measurements at the NIMS Battery Research Platform (Tsukuba, Japan).

■ REFERENCES

(1) Kato, Y.; Kawamoto, K.; Kanno, R.; Hirayama, M. Discharge Performance of All-Solid-State Battery Using a Lithium Superionic Conductor $Li_{10}GeP_2S_{12}$. *Electrochemistry* **2012**, *80* (10), 749−751.

(2) Sun, Y.; Suzuki, K.; Hori, S.; Hirayama, M.; Kanno, R. Superionic Conductors: $Li_{10+\delta}[Sn_ySi_{1-y}]_{1+\delta}P_{2-\delta}S_{12}$ with a $Li_{10}GeP_2S_{12}$-Type Structure in the Li_3PS_4-Li_4SnS_4-Li_4SiS_4 Quasi-Ternary System. *Chem. Mater.* **2017**, *29* (14), 5858−5864.

(3) Ohta, N.; Takada, K.; Zhang, L.; Ma, R.; Osada, M.; Sasaki, T. Enhancement of the High-rate Capability of Solid-state Lithium Batteries by Nanoscale Interfacial Modification. *Adv. Mater.* **2006**, *18* (17), 2226−2229.

(4) Ohta, N.; Takada, K.; Sakaguchi, I.; Zhang, L.; Ma, R.; Fukuda, K.; Osada, M.; Sasaki, T. $LiNbO_3$-Coated $LiCoO_2$ as Cathode Material for All Solid-State Lithium Secondary Batteries. *Electrochem. commun.* **2007**, *9* (7), 1486−1490.

(5) Robinson, A. L.; Janek, J. Solid-State Batteries Enter EV Fray. *MRS Bull.* **2014**, *39* (12), 1046−1047.

(6) Morino, Y.; Sano, H.; Takahashi, T.; Miyashita, N.; Sakuda, A.; Hayashi, A. Hydrogen Components of a Sulfide-Based Argyrodite-Type Solid Electrolyte after Moisture Exposure. *J. Phys. Chem. C* **2023**, *127* (28), 13616−13622.

(7) Scharmann, T.; Özcelikman, C.; Nguyen, D. M.; Heck, C. A.; Wacker, C.; Michalowski, P.; Kwade, A.; Dröder, K. Quantification of Hydrogen Sulfide Development during the Production of All-Solid-State Batteries with Argyrodite Sulfide-Based Separators. *ACS Appl. Energy Mater.* **2024**, *7* (3), 1261−1269.

(8) Thangadurai, V.; Kaack, H.; Weppner, W. J. F. Novel Fast Lithium Ion Conduction in Garnet-type $Li_5La_3M_2O_{12}$ (M = Nb, Ta). *J. Am. Ceram. Soc.* **2003**, *86* (3), 437−440.

(9) Murugan, R.; Thangadurai, V.; Weppner, W. Fast Lithium Ion Conduction in Garnet-type $Li_7La_3Zr_2O_{12}$. *Angew. Chemie Int. Ed.* **2007**, *46* (41), 7778−7781.

(10) Ramakumar, S.; Deviannapoorani, C.; Dhivya, L.; Shankar, L. S.; Murugan, R. Lithium Garnets: Synthesis, Structure, Li^+ Conductivity, Li^+ Dynamics and Applications. *Prog. Mater. Sci.* **2017**, *88*, 325−411.

(11) Dorai, A.; Kuwata, N.; Takekawa, R.; Kawamura, J.; Kataoka, K.; Akimoto, J. Diffusion Coefficient of Lithium Ions in Garnet-Type $Li_{6.5}La_3Zr_{1.5}Ta_{0.5}O_{12}$ Single Crystal Probed by ^7Li Pulsed Field Gradient-NMR Spectroscopy. *Solid State Ionics* **2018**, *327*, 18−26.

(12) Kataoka, K.; Akimoto, J. Lithium-Ion Conductivity and Crystal Structure of Garnet-Type Solid Electrolyte $Li_{7-x}La_3Zr_{2-x}Ta_xO_{12}$ Using Single-Crystal. *J. Ceram. Soc. Japan* **2019**, *127* (8), 521−526.
(13) Alpen, U. v.; Bell, M. F.; Wichelhaus, W.; Cheung, K. Y.; Dudley, G. J. Ionic Conductivity of $Li_{14}Zn(GeO_4)_4$ (Lisicon). *Electrochim. Acta* **1978**, *23* (12), 1395−1397.
(14) Okumura, T.; Takeuchi, T.; Kobayashi, H. All-Solid-State Batteries with $LiCoO_2$-Type Electrodes: Realization of an Impurity-Free Interface by Utilizing a Cosinterable $Li_{3.5}Ge_{0.5}V_{0.5}O_4$ Electrolyte. *ACS Appl. Energy Mater.* **2021**, *4* (1), 30−34.
(15) Zhao, G.; Suzuki, K.; Okumura, T.; Takeuchi, T.; Hirayama, M.; Kanno, R. Extending the Frontiers of Lithium-Ion Conducting Oxides: Development of Multicomponent Materials with γ-Li_3PO_4-Type Structures. *Chem. Mater.* **2022**, *34* (9), 3948−3959.
(16) Watanabe, K.; Tashiro, A.; Ichinose, Y.; Takeno, S.; Suematsu, K.; Mitsuishi, K.; Shimanoe, K. Lowering the Sintering Temperature of $Li_7La_3Zr_2O_{12}$ Electrolyte for Co-Fired All-Solid-State Batteries via Partial Bi Substitution and Precise Control of Compositional Deviation. *J. Ceram. Soc. Japan* **2022**, *130* (7), 416−423.
(17) Akimoto, J.; Akao, T.; Nagai, H.; Kataoka, K. Low-Temperature Sintering of a Garnet-Type $Li_{6.5}La_3Zr_{1.5}Ta_{0.5}O_{12}$ Solid Electrolyte and an All-Solid-State Lithium-Ion Battery. *ACS Appl. Mater. Interfaces* **2023**, *15* (15), 18973−18981.
(18) Yoshida, N.; Kuwata, N.; Hasegawa, G.; Takada, K. Liquid Phase Penetration Sintering of Garnet-Type Solid Electrolyte LLZTO. *Solid State Ionics* **2023**, *403*, 116408.
(19) Hayashi, N.; Watanabe, K.; Shimanoe, K. Co-Sintering a Cathode Material and Garnet Electrolyte to Develop a Bulk-Type Solid-State Li Metal Battery with Wide Electrochemical Windows. *J. Mater. Chem. A* **2024**, *12* (9), 5269−5281.
(20) Kim, J.; Kim, J.; Avdeev, M.; Yun, H.; Kim, S.-J. $LiTa_2PO_8$: A Fast Lithium-Ion Conductor with New Framework Structure. *J. Mater. Chem. A* **2018**, *6* (45), 22478−22482.
(21) Ishigaki, N.; Kataoka, K.; Morikawa, D.; Terauchi, M.; Hayamizu, K.; Akimoto, J. Structural and Li-Ion Diffusion Properties of Lithium Tantalum Phosphate $LiTa_2PO_8$. *Solid State Ionics* **2020**, *351*, 115314.
(22) Ishigaki, N.; Kataoka, K.; Morikawa, D.; Terauchi, M.; Hayamizu, K.; Akimoto, J. Corrigendum to "Structural and Li-Ion Diffusion Properties of Lithium Tantalum Phosphate $LiTa_2PO_8$" [Solid State Ion. 351 (August 2020) 115314] (Solid State Ionics (2020) 351, (S0167273820300977), (10.1016/j.Ssi.2020.115314)). *Solid State Ionics* **2020**, *354*, 115421.
(23) Hussain, F.; Li, P.; Li, Z. Theoretical Insights into Li-Ion Transport in $LiTa_2PO_8$. *J. Phys. Chem. C* **2019**, *123* (32), 19282−19287.
(24) Kim, R.; Miara, L. J.; Kim, J.-H.; Kim, J.; Im, D.; Wang, Y. Computational Design and Experimental Synthesis of Air-Stable Solid-State Ionic Conductors with High Conductivity. *Chem. Mater.* **2021**, *33* (17), 6909−6917.
(25) Dai, R.; Avdeev, M.; Kim, S.-J.; Prasada Rao, R.; Adams, S. Temperature Dependence of Structure and Ionic Conductivity of $LiTa_2PO_8$ Ceramics. *Chem. Mater.* **2022**, *34* (23), 10572−10583.
(26) Kwatek, K.; Ślubowska-Walkusz, W.; Nowiński, J. L.; Jastrzębski, C.; Krawczyńska, A. T.; Sobrados, I.; Diez-Gómez, V.; Sanz, J. Superior Ionic Conductivity of Zr-Doped $LiTa_2PO_8$ Ceramics. *Acta Mater.* **2024**, *276*, 120125.
(27) Lei, J.; Liu, Z.; Wang, H.; Li, Z.; Liao, R.; Dmytro, S.; Zhang, Q. Te Doping Effect on the Structure and Ionic Conductivity of $LiTa_2PO_8$ Solid Electrolyte. *Ceram. Int.* **2023**, *49* (2), 1980−1986.
(28) Lei, J.; Liu, Z.; Li, Z.; Wang, H.; Dmytro, S.; Zhang, Q. Characterization of Ce-Doped $LiTa_2PO_8$ with Improved Stability to Lithium and Ionic Conductivity. *J. Energy Storage* **2023**, *72*, 108080.
(29) Kresse, G.; Furthmüller, J. Efficient Iterative Schemes for Ab Initio Total-Energy Calculations Using a Plane-Wave Basis Set. *Phys. Rev. B* **1996**, *54* (16), 11169−11186.
(30) Kresse, G.; Joubert, D. From Ultrasoft Pseudopotentials to the Projector Augmented-Wave Method. *Phys. Rev. B* **1999**, *59* (3), 1758−1775.
(31) Perdew, J. P.; Burke, K.; Ernzerhof, M. Generalized Gradient Approximation Made Simple. *Phys. Rev. Lett.* **1996**, *77* (18), 3865−3868.
(32) Tanner, J. E. Use of the Stimulated Echo in NMR Diffusion Studies. *J. Chem. Phys.* **1970**, *52* (5), 2523−2526.
(33) Stejskal, E. O.; Tanner, J. E. Spin Diffusion Measurements: Spin Echoes in the Presence of a Time-dependent Field Gradient. *J. Chem. Phys.* **1965**, *42* (1), 288−292.
(34) Santoro, A.; Roth, R. S.; Minor, D. Neutron Powder Diffraction Study of the Intermediate-Temperature Form of Lithium Tantalum Oxide. *Acta Crystallogr. Sect. B Struct. Crystallogr. Cryst. Chem.* **1977**, *33* (12), 3945−3947.
(35) Aono, H.; Sugimoto, E.; Sadaoka, Y.; Imanaka, N.; Adachi, G. Electrical Properties and Crystal Structure of Solid Electrolyte Based on Lithium Hafnium Phosphate $LiHf_2(PO_4)_3$. *Solid State Ionics* **1993**, *62* (3−4), 309−316.
(36) Martínez-Juárez, A.; Pecharromán, C.; Iglesias, J. E.; Rojo, J. M. Relationship between Activation Energy and Bottleneck Size for Li^+ Ion Conduction in NASICON Materials of Composition $LiMM'(PO_4)_3$; M, M′ = Ge, Ti, Sn, Hf. *J. Phys. Chem. B* **1998**, *102* (2), 372−375.
(37) Morin, E.; Le Mercier, T.; Quarton, M.; Losilla, E. R.; Aranda, M. A. G.; Bruque, S. Neutron Powder Diffraction Data for Low- and High-Temperature NASICON Phases of $LiM_2(PO_4)_3$ (M = Hf, Sn). *Powder Diffr.* **1999**, *14* (1), 53−60.
(38) Martínez-Juárez, A.; Iglesias, J. E.; Rojo, J. Ionic Conductivity of NASICON-Type $LiHf_2(PO_4)_3$: A Reexamination. *Solid State Ionics* **1996**, *91* (3−4), 295−301.
(39) Kuwata, N.; Lu, X.; Miyazaki, T.; Iwai, Y.; Tanabe, T.; Kawamura, J. Lithium Diffusion Coefficient in Amorphous Lithium Phosphate Thin Films Measured by Secondary Ion Mass Spectroscopy with Isotope Exchange Methods. *Solid State Ionics* **2016**, *294*, 59−66.
(40) Hasegawa, G.; Kuwata, N.; Hashi, K.; Tanaka, Y.; Takada, K. Lithium-Ion Diffusion in Perovskite-Type Solid Electrolyte Lithium Lanthanum Titanate Revealed by Pulsed-Field Gradient Nuclear Magnetic Resonance. *Chem. Mater.* **2023**, *35* (10), 3815−3824.
(41) Murch, G. E. The Haven Ratio in Fast Ionic Conductors. *Solid State Ionics* **1982**, *7* (3), 177−198.
(42) Van der Ven, A.; Deng, Z.; Banerjee, S.; Ong, S. P. Rechargeable Alkali-Ion Battery Materials: Theory and Computation. *Chem. Rev.* **2020**, *120* (14), 6977−7019.
(43) Compaan, K.; Haven, Y. Correlation Factors for Diffusion in Solids. *Trans. Faraday Soc.* **1956**, *52* (6), 786−801.

https://doi.org/10.1021/acsaem.4c01773
ACS Appl. Energy Mater. 2024, 7, 10897−10905